Airborne Doppler Radar Observations of Tropical Cyclone Boundary Layer Kinematic Structure and Evolution During Landfall

Robert F. Rogers[1] and Jun A. Zhang[1,2]

[1]NOAA/OAR/Atlantic Oceanographic and Meteorological Laboratory/Hurricane Research Division

Miami, FL

[2]University of Miami/Cooperative Institute for Marine and Atmospheric Studies

Miami, FL

To be submitted to *Geophysical Research Letters*

July 2023

Key Points

- Wind asymmetries in tropical cyclone boundary layer are governed by TC motion, vertical shear over open water; frictional effects at landfall
- Boundary layer radial inflow peaks in the offshore-flow side at landfall, peak in tangential winds at top of boundary layer occurs on the onshore-flow side
- These observations are largely consistent with recent numerical modeling studies of tropical cyclone landfall

Abstract

Airborne Doppler radar observations of the wind field in the tropical cyclone boundary layer (TCBL) during the landfall of Hurricane Ida (2021) are examined here. Asymmetries in tangential and radial flow are governed by TC motion and vertical wind shear prior to landfall, while frictional effects dominate the asymmetry location during landfall. Strong TCBL inflow on the offshore-flow side of Ida occurs during landfall, while the location of the peak tangential wind at the top of the TCBL during this period is located on the onshore-flow side. A comparison of these observations with a numerical simulation of TC landfall shows many consistencies with the modeling study, though there are some notable differences that may be related to differences in the characteristics of the land surface between the simulation and the observations.

Plain Language Summary

The structure of the wind field in the lowest levels of a hurricane when it makes landfall plays a significant role in determining damage. This study uses aircraft observations to document

the changes that occur in the winds in the lowest levels of a hurricane prior to and as it makes landfall. The location of the strongest inflow into the storm center and winds around the center are determined by characteristics like storm motion and environmental winds when the storm is over open water, but at landfall these wind peaks are dominated by the differences in friction between the land surface and water. At landfall, the inflow near the surface is strongest on the side of the hurricane experiencing offshore flow, while winds moving around the storm center a few thousand feet above the surface are strongest on the side experiencing onshore flow. These results are mostly consistent with computer modeling studies, allowing for studies on physical processes to be conducted using these models.

Key words

Hurricane landfall

Boundary layer winds

Aircraft observations

1. Introduction

The wind field in the tropical cyclone (TC) boundary layer (BL) determines the magnitude and distribution of surface enthalpy and momentum fluxes, which is critical in determining whether a TC will intensify (Ooyama 1969; Emanuel 1986, 1995, 1999; Shay et al. 2000; Cione et al. 2013; Jaimes et al. 2015; Zhang et al. 2017; Wadler et al. 2021). Decomposing the TCBL wind field into tangential and radial components also yields important insights into other intensity change processes, such as the radial advection of angular momentum and radial mass flux within and above the frictional inflow layer, as well as factors affecting the wind structure in the TCBL, such as the azimuthal distribution of supergradient flow and the presence of TCBL jets (Smith and Montgomery 2015, Smith et al. 2009, 2021). Additionally, TCBL winds govern storm surge and rainfall fields at landfall. Understanding the physical processes that govern the structure and evolution of TCBL winds is therefore critical to predict TC structure and intensity as well as impacts at landfall.

Past observational and modeling studies have characterized the symmetric structures of TCBL flow over the open ocean (Kepert 2001; Kepert and Wang 2001; Bell and Montgomery 2008; Zhang et al. 2011, 2015, 2023; Bryan 2012; Rogers et al. 2012; Sanger et al. 2014; Montgomery et al. 2014; Ming et al. 2015; Ahern et al. 2019), finding that inflow is maximized in the lowest 200 m, with a region of weaker inflow at the top of and above the TCBL. The depth of the inflow layer increases with increasing radial distance from the TC center. Peak tangential wind occurs in the inflow layer, and there is a region of supergradient flow at and inside the region of strongest inflow.

The dominant drivers of azimuthal asymmetries in TCBL winds over the open ocean are TC motion (Shapiro et al. 1983, Ueno et al. 2009, 2011; Zhang and Uhlhorn 2012; Uhlhorn et al.

2014) and vertical wind shear (Rogers and Uhlhorn 2007; Zhang et al. 2013; Reasor et al. 2013; Uhlhorn et al. 2014; Klotz and Jiang 2017; Sun et al. 2019; Ming et al. 2022). TC motion establishes a region of strong TCBL tangential flow to the right of storm motion and maxima in radial inflow and convergence in the TCBL in the front and front-right quadrants (Shapiro 1983). Vertical shear establishes peak tangential wind speed, inflow, and convergence in the downshear and downshear-left quadrants (Zhang et al. 2013; Reasor et al. 2013; Uhlhorn et al. 2014).

Several observational studies have examined the variation of the TCBL wind field and features at and after landfall. The kinematic boundary layer height is reduced with decreases in distance from the TC center, and maximum BL wind is larger in an offshore regime in the eyewall region compared to an onshore regime (Giammanco et al. 2013). Roll-like features were documented during TC landfalls using Doppler radar and tower data (e.g., Wurman and Winslow 1998; Kosiba and Wurman 2014; Lorsolo et al. 2008; Zhu et al. 2010). Ming et al. (2014) observed enhancement of turbulence kinetic energy by convective downdrafts in the BL of Typhoon Morakot (2009) near rainbands, while the strongest surface winds during the landfall of Hurricane Harvey (2017) were found to be associated with convective perturbations in the eyewall (Alford et al. 2019; Fernadez-Caban et al. 2019). Alford et al. (2020) investigated the coastal transition of vertical wind profiles in the BL of Hurricane Irene (2011) and found that the tangential wind maximum was within the inflow layer over water but was above the inflow layer onshore. The tangential wind maximum was within the inflow layer from the coastline up to 5 km inland, which is the transition zone between ocean and land exposure. The height of the maximum radial wind increases from water to land in response to the growth of the internal boundary layer that forms in the transition zone due to flow adjustment to the surface roughness change (Hirth et al. 2004; Alford et al. 2020).

Clearly, as a TC approaches land, variations in surface roughness dominate the creation of asymmetries. It is important to understand how these asymmetries affect the wind field in the TCBL at landfall, as these structures are what determine the hazards driven by wind, storm surge, and rainfall. Many of the landfall papers described above, however, focus on TCBL structure and evolution at specific ground-relative locations, because that is where the instruments are located. They focus less on the evolution of the flow field in a storm-relative framework, and they say little about the flow field when the TC is > 100 km offshore.

A recent paper by Hlywiak and Nolan (2022, hereafter HN22) examined the structure and evolution of asymmetries in the TCBL wind field in a storm-relative framework prior to and during landfall using an idealized model. In their simulation they found an increase in the strength of the radial inflow on the offshore flow side of the TC, beginning when the TC was about 200 km offshore. They attributed the increase in radial inflow to the decrease in frictional stress once the agradient offshore flow crossed the coastline and reached water. An enhanced advection of angular momentum by the secondary circulation, tied to the strengthened radial inflow in the TCBL on the offshore flow side, additionally forced a strengthening of a supergradient jet near the top of the TCBL, resulting in a maximum in wind speed downstream; i.e., on the onshore flow side at the top of the TCBL. They compared some of their modeling results to a set of buoy observations of near-surface inflow angle from three landfalling TCs and found general agreement with their results.

The comparisons with observations from HN22 were limited, however, to a relatively small number of point observations at the surface, with no information on the variation of the tangential and radial flow with height and as a function of distance from the storm center. A comparison of the three-dimensional structure of the flow field in the TCBL, and its variation

between when a TC is well offshore and when it is making landfall, would provide a more robust evaluation of HN22's results. Ground-based radar could provide such a comparison, but the elevation of the beam and curvature of the Earth would prevent observations of the wind field in the lowest 1-2 km, except when the TC is close (< 100 km) to the radar site.

Airborne Doppler radar data, by contrast, can provide a comprehensive depiction of the structure and evolution of the flow field by sampling the TC at many different periods during its approach to landfall. In this study, profile analyses (e.g., Rogers et al. 2012; Zhang et al. 2023) from airborne Doppler radar onboard the NOAA WP-3D aircraft (hereafter P-3) are used to produce analyses of tangential and radial wind in a narrow (~10-km wide) swath under the aircraft with 150 m spacing in the vertical and down to altitudes as low as 150 m above the surface. Three-dimensional radar analyses that provide winds and reflectivity in a swath extending approximately 50 km in either direction normal to the flight track, with 500 m spacing in the vertical, will also be used. Together, these radar analyses will be used to examine the structure of TCBL tangential and radial flow in Hurricane Ida as it made landfall along the coastline of Louisiana in August 2021. The analysis shown here will provide an opportunity to evaluate results from HN22 in a more comprehensive and robust manner than what was shown in their study. It will also provide the opportunity to assess the evolution of TCBL flow fields as Ida transitioned from an over-water exposure to one associated with landfall.

2. Case description

Ida formed from a tropical wave that moved into the southwest Caribbean (Beven et al. 2022), tracked northwest and was declared a tropical depression on August 26, and became a hurricane prior to its first landfall in western Cuba on August 27. Once Ida emerged into the

154 southeastern Gulf of Mexico, a favorable environment and inner-core structure allowed Ida to
155 strengthen rapidly, intensifying from 70 to 130 kt in the 24-h period from 1200 UTC 28 August
156 to 1200 UTC 29 August. By the end of this period of rapid intensification, Ida was southwest of
157 the mouth of the Mississippi River. A continued northwest motion brought Ida inland near Port
158 Fouchon, Louisiana, at 1655 UTC 29 August.

159 NOAA P-3 aircraft N42RF sampled Ida during its track across the Gulf of Mexico up to
160 landfall. The focus of the analysis in this study will be on the final two missions of N42RF into
161 Ida. Flight tracks for these missions are shown in Fig. 1. The first mission, with mission ID
162 20210828H (hereafter 28H), occurred from 1955 UTC 28 to 0156 UTC 29 August, when Ida
163 was in the eastern Gulf of Mexico and ~300 km prior to landfall. During this time Ida was
164 tracking toward the northwest at 14 kt and was experiencing 850-200 hPa vertical shear of ~5 kt
165 with a shear heading nearly due east. The mission consisted of a set of radial passes through the
166 center of Ida at different azimuthal locations, beginning and ending in the northeast quadrant.
167 The second mission, 20210829H (hereafter 29H), occurred during landfall from 1703 UTC to
168 2304 UTC 29 August. This mission began with a flight leg paralleling the southeast coast of
169 Louisiana, flying inbound to the center from the east-northeast, through the center as Ida was
170 making landfall, and outbound from the center toward the west-southwest. This leg, extending
171 from points 1 to 2 from 29H in Fig. 1, is termed a “coastal run”, and it will be used to examine
172 variations in offshore and onshore flow structures later. The aircraft then flew away from the
173 coast and flew an inbound leg toward the center in the southwest quadrant and an outbound leg
174 in the southeast quadrant before finishing its pattern well-removed to the southeast of the TC
175 center. During the landfall mission

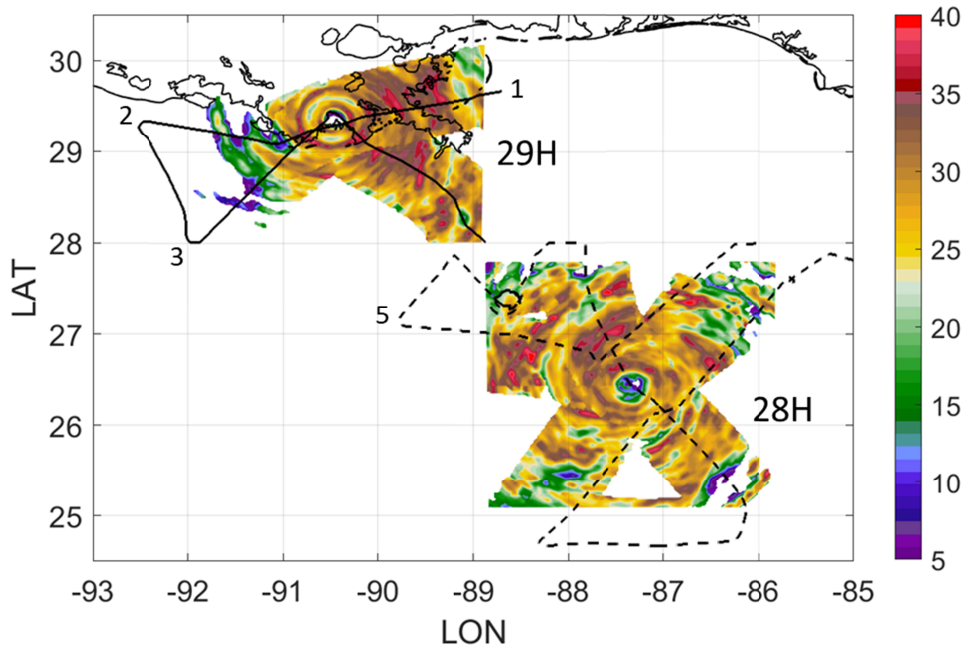

Figure 1. Radar reflectivity (shaded, dBZ) at 4-km altitude obtained from merged analyses of tail Doppler radar on the P-3 aircraft during the 28H and 29H missions (labeled). Flight tracks for each mission are overlain, with dashed (solid) lines denoting the flight track for 28H (29H). Numbers on each flight track denote initial point, key turn points, and final point for each pattern.

Ida was tracking toward the north-northwest at a slower translation speed (9 kt), and the vertical shear had increased slightly to ~8 kt with a heading toward the east-southeast.

3. Results

Plots of radar reflectivity from 28H and 29H (cf. Fig. 1) show the well-developed inner core of Ida during the two missions. Ida's eye during the 28H mission was large, with a radar-defined diameter of ~60 km and broad swaths of high reflectivity and heavy rainfall in all quadrants of the TC. For the 29H mission, Ida's eye had contracted to ~30 km diameter. There was also an indication of an outer eyewall in the reflectivity field at ~60 km radius from the TC

192 center. Additional rainband activity was apparent further outward on the east side of the TC. On
193 the west and southwest side, reflectivity outside the inner core was less widespread.

194 Plots of earth-relative tangential wind at 0.5 km and 2 km altitude from the three-
195 dimensional radar analyses are shown in Fig. 2. The increase in tangential winds associated with
196 Ida's intensification up to landfall is clearly seen here. Of particular interest is the azimuthal
197 location of peak tangential winds at each altitude. For 28H, when Ida was over water, the peak
198 wind speeds are located in the eyewall north-northeast of the TC center within the TCBL (i.e.,
199 0.5 km). The peak winds at the top of the TCBL (i.e., 2 km) are rotated upwind, northeast of the
200 TC center at this time. During 29H, when Ida was making landfall, there is a significant change
201 in the azimuthal location of the peak tangential winds. Within the TCBL the strongest winds are
202 to the south and southeast of the TC center, with an azimuthal shift of >90 degrees clockwise
203 from 28H. The direction of the storm motion heading (vertical shear) changed by ~10 (30)
204 degrees between 28H and 29H, so the shift in the azimuthal location of the peak tangential winds
205 does not appear to be driven, at least primarily, by changes in storm motion or vertical shear
206 direction. Rather, the change in the azimuthal location of TCBL tangential winds at landfall is
207 likely due to the adjustment of the winds as they exit the higher roughness values over land to the
208 lower roughness over water on the offshore-flow (i.e., west) side of the TC, similar to that shown
209 in HN22. At the top of the TCBL, the strongest winds remain to the northeast of the TC center,
210 extending from the coast to locations well inland.

211 Characteristics of the radial flow within the TCBL are shown in the Doppler profile
212 analyses in Fig. 3. Figure 3a shows vertical cross sections in the lowest 2 km for radial flow
213 along a southwest/northeast-oriented radial pass during 28H. The maximum inflow on this pass
214 (> 15 m s^{-1}) is seen in the leg in the northeast quadrant. This location is to the right of the storm

motion heading and to the left of the vertical shear heading, an orientation consistent with previous studies relating boundary-layer inflow and storm motion/vertical shear. Figure 3b shows a similar profile, but along the coastline (during the "coastal run" leg, from point 1-2 shown in Fig. 1) during 29H. Now the radial inflow has shifted and is maximized on the west (offshore-flow) side of the TC, located ~40-50 km from the TC center, where values of peak inflow are ~20 m s^{-1}. On the east (onshore-flow) side, inflow magnitude is about half of that seen on the offshore-flow side at similar radii, though there is a weaker local maximum of inflow at about 80 km, likely associated with the outer eyewall seen in Fig. 1. This relationship between the peak radial inflow in the offshore vs. onshore-flow sides of the TC is consistent with HN22, who argued that the increase in the radial inflow in the offshore flow is attributed to the sudden decrease in frictional stress once the highly agradient flow crosses the coastline.

A depiction of the azimuthal variation of TCBL inflow strength, and how it varies from 28H to 29H, is shown in Figs. 3c and 3d. Here the radial inflow is averaged within predefined boxes that include the radius of maximum wind (RMW) and the lowest 150 km of the profile analysis for each radial pass through the TC center for both missions. These values are then plotted as a function of azimuth, with the TC motion and vertical shear heading vectors included for reference. During 28H the peak radial inflow in the lowest 150-300 m layer is in the northeast portion of the TC, to the east (right) of the storm motion vector and to the west (left) of the vertical shear vector. Such an orientation of inflow with respect to the TC motion and shear vectors over open water is consistent with the studies mentioned earlier and shown in Fig. 3a. For 29H, the orientation of radial inflow changes significantly. The strongest inflow now is on the west side of the storm. In terms of its orientation relative to the motion and shear vectors, the peak inflow in

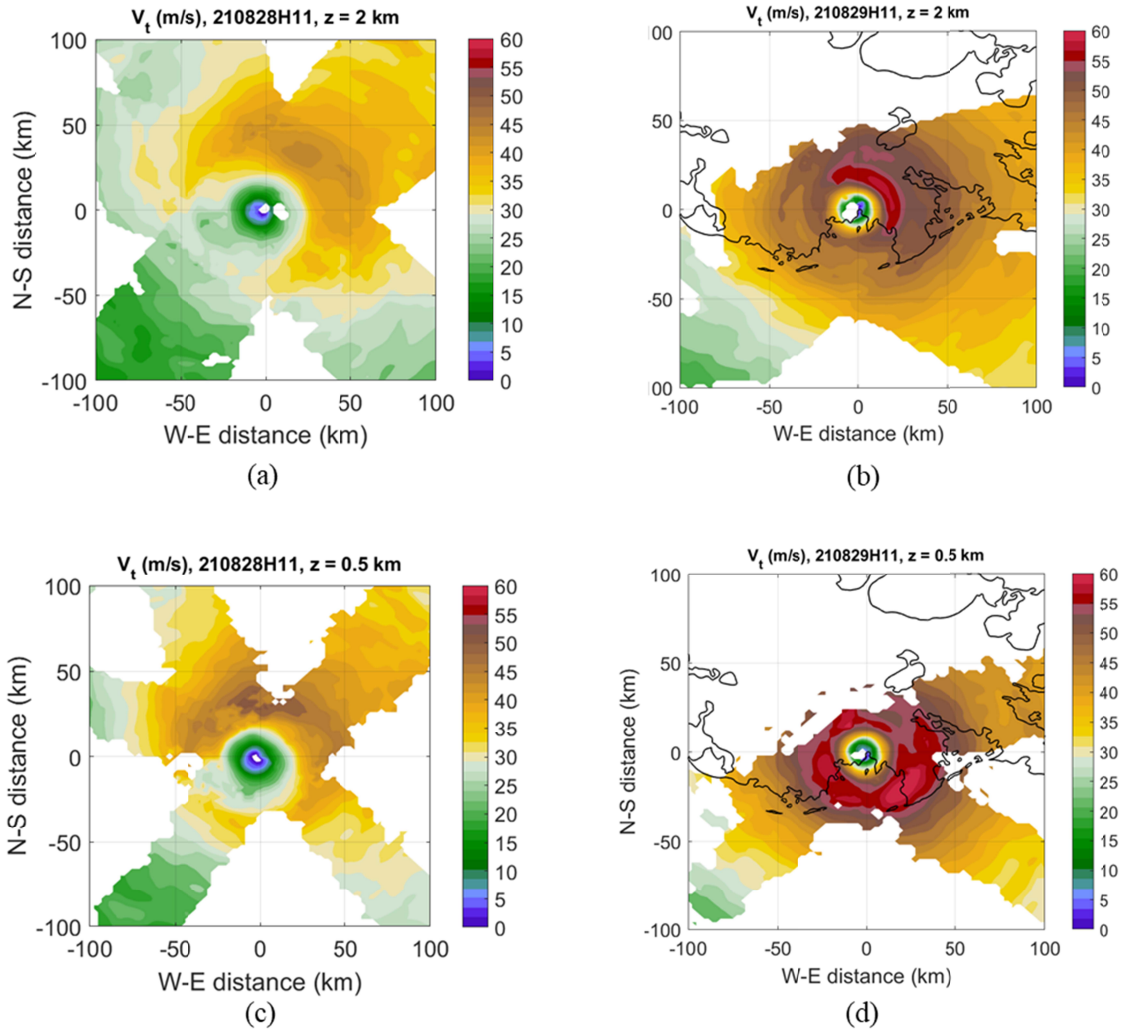

Figure 2. Earth-relative tangential wind (shaded, m s^{-1}) at 2 km altitude (top of TCBL) for (a) 28H and (b) 29H missions. Tangential winds at 0.5 km altitude (within TCBL) also shown for (c) 28H and (d) 29H missions.

the TCBL is nearly opposite the shear vector and located about 90 degrees to the left of the motion vector – orientations at odds with the expected azimuthal location over open water based on motion and shear considerations alone. The peak inflow is located on the offshore- flow side of the TC. Such an orientation is consistent with HN22's results, and suggests that landfall impacts, resulting from changes in the roughness length as air moves from over-land to over-

water exposures, take on a greater significance in governing inflow structure than with TC motion and shear. The increase in inflow between 28H and 29H on the west and southwest sides of the storm – from about 5 m s-1 during 28H to 8-10 m s-1 during 29H – provide a potential explanation for the azimuthal location of the peak tangential winds in the southeast quadrant during 29H. The greater inward advection of angular momentum in the stronger inflow within the TCBL on the west and southwest sides during 29H lead to an enhancement in the tangential wind at the top of the TCBL

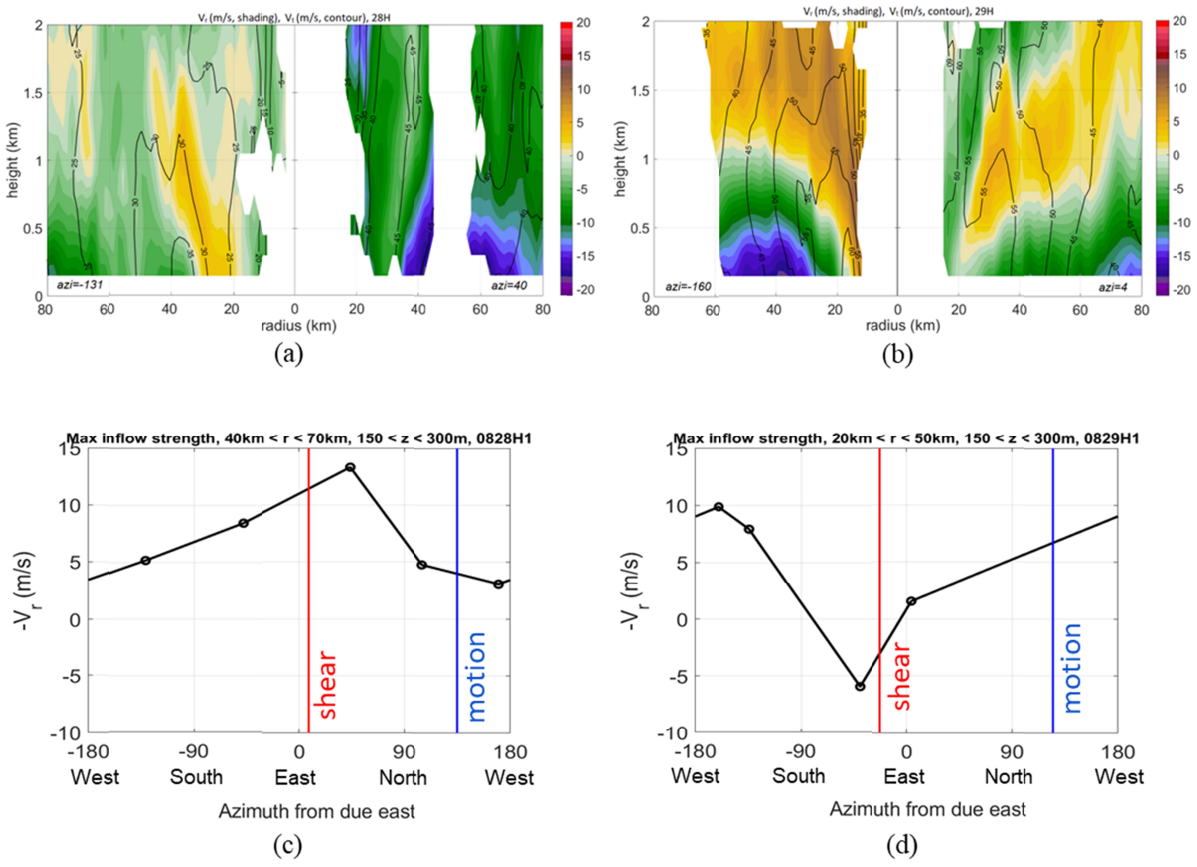

Figure 3. (a) Earth-relative tangential wind (contour, m s^{-1}) and radial wind (shaded, m s^{-1}) from southwest/northeast-oriented profile analysis from tail Doppler radar during 28H. (b) As in (a), but for the coastal run during 29H. (c) Azimuthal variation of areally-averaged near-surface radial inflow (see text for calculation details; positive values denote inflow) for radial passes during 28H. Storm motion and vertical shear heading denoted. (d) as in (c), but for 29H.

downwind; i.e., in the southeast quadrant. Such an explanation is consistent with that described in HN22. The variation of tangential and radial flow with height and azimuth for 28H and 29H is shown in azimuth-height transects ("curtain plots" in HN22) in Fig. 4 using the three-dimensional Doppler radar analyses. Here the tangential and radial wind is averaged in a curtain of 30 km radial width around the TC center, with the inner radius corresponding to the 2-km RMW that thus

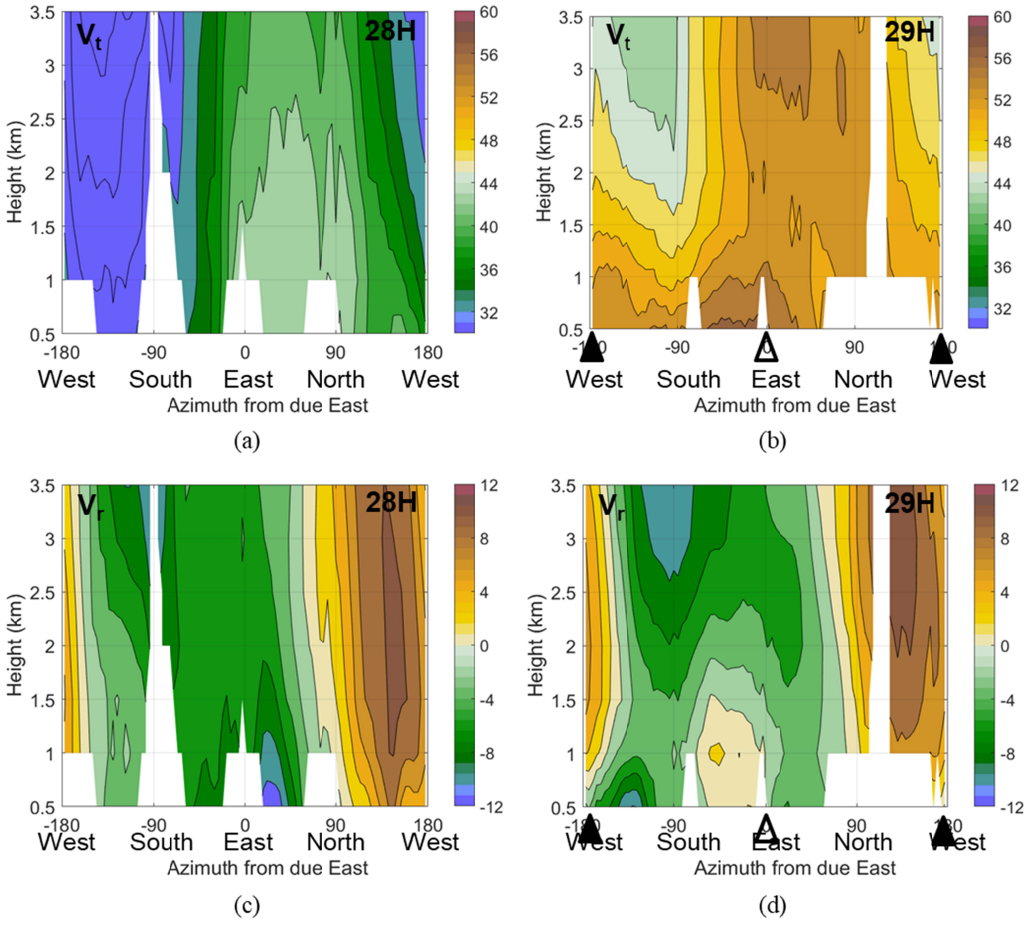

Figure 4. Azimuth-height plots (see text for calculation details) of earth-relative tangential winds (shaded, m s^{-1}) for (a) 28H and (b) 29H. (c) As in (a), but for earth-relative radial winds (shaded, m s^{-1}, negative values denote inflow). (d) As in (c), but for 29H. Triangles in (b) and (d) denote locations of coastline, with filled (unfilled) triangles denoting offshore (onshore) flow.

includes flow features at and outside the RMW, similar to Fig. 8 in HN22. Over open water, the tangential wind shows a clear wavenumber-1 pattern, with the peak values uniformly located in the northeast quadrant, from 0.5 to 3.5 km altitude. The radial flow shows a similar wavenumber-1 type pattern, with strongest inflow above the TCBL located south of the TC center and within the TCBL located east-northeast of the TC center. At landfall, the tangential and radial inflow maxima generally remain at the same location above the TCBL altitude as 28H. However, the locations of the maxima within the TCBL have both shifted significantly, with the tangential wind maximum shifting from the northeast quadrant in 28H to the southeast quadrant in 29H, and the radial inflow maximum shifting from the east side in 28H to the southwest quadrant in 29H. The depth of the changes in tangential and radial flow are ~1-1.5 km, suggesting this is the depth over which the frictional effects on radial and tangential flow described above are dominant.

4. Discussion

The results shown here present an opportunity to use observations to explore the structure and evolution of the TCBL during landfall, while also providing the ability to assess the results of HN22. Many of the structures seen from airborne Doppler radar during Ida's landfall are similar to those shown in their paper. The strongest tangential flow is located on the onshore-flow side within and above the TCBL for both HN22 and Ida (cf. Figs. 2, 4). Peak radial inflow during landfall in the TCBL is located at and just downwind of the offshore-flow (cf. Figs. 3, 4), similar to that shown in HN22, and the location of peak inflow shifts downwind, further offshore, with height above the TCBL in both HN22 and Ida (cf. Fig. 4).

298 The relationship between the tangential and radial inflow peaks during Ida's landfall
299 suggests a similar set of processes as that described in HN22. The peak in radial inflow in the
300 offshore flow is likely related to the sudden decrease in frictional stress when the agradient flow
301 crosses the coastline. Enhanced advection of angular momentum by this inflow forces a
302 strengthening of the supergradient jet near the top of the TCBL, downwind of the peak inflow.
303 Such a relationship is seen by the downwind rotation of the azimuthal location of peak inflow
304 and tangential wind shown in Figs. 4b, d.

305 An important result shown here is the comparison of the vertical structure of the wind
306 asymmetries in Fig. 4, which showed the depth over which these wind field modifications occur.
307 Prior to landfall, the inflow peak extends up to ~1.5 km altitude on the east-northeast side of the
308 storm. During landfall, the inflow peak shifts to the west (offshore) side of the TC. This shift
309 extends up to about 1-1.5 km altitude. The depth over which this shift occurs is generally
310 consistent with the TCBL depth as defined by the turbulent kinetic energy field found in HN22.

311 While many of the results shown here support the results from HN22, there are some
312 ways that the results differ. For example, the location of peak tangential wind in Ida at the top of
313 the TCBL is in the northeast quadrant at landfall (cf. Figs. 2, 4). This location is inland, and it
314 contrasts with the results from HN22, who showed that the tangential wind peak at the top of the
315 TCBL is located in the right-rear quadrant relative to landfall; i.e., offshore. It is not clear what
316 the reason is for this difference. The TC in HN22 was ~140 kt, while Ida was 125 kt at landfall,
317 so it does not appear that storm intensity played a significant role in explaining the difference.
318 The roughness length of the swampy marshlands of the Louisiana coast is ~0.05 cm, while the
319 roughness lengths used in HN22 ranged between 5 and 50 cm. The sensitivity tests shown in
320 HN22 showed that increasing the inland roughness length led to stronger inflow in the offshore

flow, stronger inward advection of angular momentum, and more supergradient flow at the top of the TCBL in the offshore quadrants of their simulated TCs. It is possible that, with a much smaller roughness length for Ida, the inward advection of angular momentum and supergradient flow was weaker than HN22, though that still does not explain why the maximum in tangential wind was seen further downstream (in fact inland) compared with HN22's results. Further analysis and additional sensitivity tests could shed more light on these differences.

The analysis shown here extends upon that shown in HN22 by highlighting the changing importance of various physical processes in governing the structure of surface wind asymmetries prior to and during landfall. The location of the peak tangential wind and inflow is on the northeast side of Ida prior to landfall – to the right of the storm motion vector and to the left of the vertical shear vector, consistent with past studies examining the relationship between storm motion, vertical shear, and surface wind asymmetries. As Ida makes landfall, the location of the asymmetries shifts significantly, indicating the dominant effect of frictional differences in governing the structure of asymmetries in the wind field within and at the top of the TCBL at landfall.

By providing observations of the three-dimensional structure of the wind field and its variation in time, the results shown here extend upon those comparisons shown in HN22. HN22 uses buoy observations to compare inflow angles with their simulations. These buoys are fixed points in space, though they do provide time continuity. By contrast, the radar observations shown here show a fully three-dimensional field (subject to presence of scatterers), but these fields are essentially snapshots in time. Ideally, a combination of these types of observing systems would provide both spatial coverage and temporal continuity.

343 Additional cases, including more aircraft missions sampling TCs with a similar "coastal
344 run" pattern during landfall, are needed to assess the robustness of the results shown here. An
345 incorporation of land-based observational systems, similar to those studies described above,
346 could fill in gaps in coverage from the aircraft (see, e.g., the lack of TCBL observations on the
347 north and northwest sides of Ida in 29H) and provide observations of roll vortices, eye-eyewall
348 mesovortices, and convective downdrafts and associated gusts to provide an unprecedented
349 picture of the structure and evolution of the TCBL wind field and turbulent kinetic energy prior
350 to, during, and after landfall. Such an analysis is crucial to assessing damage potential for
351 landfalling TCs, from both wind and surge.
352
353 **Acknowledgements**
354 This work was supported by NOAA Base Funds, ONR TCRI Award N00014-20-1-2071,
355 NOAA Grants NA21OAR4590370, NA22OAR4590178, and NA22OAR4050669D, and
356 National Science Foundation (NSF) Awards 2228299 and 2211308.
357
358 **Data availability statement**
359 The observational data used in this paper can be accessed through
360 https://www.aoml.noaa.gov/hrd/data_sub/hurr.html.
361
362 **References**
363 Ahern, K., M.A. Bourassa, R.E. Hart, J.A. Zhang, and R.F. Rogers, 2019: Observed Kinematic
364 and Thermodynamic Structure in the Hurricane Boundary Layer during Intensity Change.
365 *Mon. Wea. Rev.*, **147**, 2765–2785, https://doi.org/10.1175/MWR-D-18-0380.1.

366 Alford, A. A., M. I. Biggerstaff, G. D. Carrie, J. L. Schroeder, B. D. Hirth, and S. M. Waugh,
367 2019: Near-surface maximum winds during the landfall of Hurricane Harvey. *Geophys. Res.*
368 *Lett.*, **46**, doi:10.1029/2018GL080013.
369 Alford, A. A., Zhang, J. A., Biggerstaff, M. I., Dodge, P., & Bodine, D. J., 2020. Transition of
370 the hurricane boundary layer during the landfall of hurricane irene (2011). *Journal of the*
371 *Atmospheric Sciences*, *77(10)*, 3509-3531.
372 Bell, M. M., and M. T. Montgomery, 2008: Observed Structure, Evolution, and Potential
373 Intensity of Category 5 Hurricane Isabel (2003) from 12 to 14 September. *Mon. Wea. Rev*.,
374 **136**, 2023–2046, https://doi.org/10.1175/2007MWR1858.1.
375 Beven, J.L., A. Hagen, and R. Berg, 2022: National Hurricane Center Tropical Cyclone Report:
376 Hurricane Ida (26 August - 1 September 2021). Report AL092021, 163 pp,
377 https://www.nhc.noaa.gov/data/tcr/AL092021_Ida.pdf
378 Bryan, G. H., (2012). Effects of surface exchange coefficients and turbulence length scales on
379 the intensity and structure of numerically simulated hurricanes. *Monthly Weather Review*,
380 *140*, 1125–1143.
381 Cione, J.J., E.A. Kalina, J.A. Zhang, and E.W. Uhlhorn, 2013: Observations of Air–Sea
382 Interaction and Intensity Change in Hurricanes. Mon. Wea. Rev., 141, 2368–2382.
383 Emanuel, K.A., 1986: An Air-Sea Interaction Theory for Tropical Cyclones. Part I: Steady-State
384 Maintenance. *J. Atmos. Sci.*, 43, 585–605.
385 Emanuel, K. A. (1995). Sensitivity of tropical cyclones to surface exchange coefficients and a
386 revised steady-state model incorporating eye dynamics. *Journal of the Atmospheric Science*,
387 **52**, 3969–3976.
388 Emanuel, K. A., 1999: Thermodynamic control of hurricane intensity. *Nature*, **401**, 665–669.

389 Fernandez-Caban, P. L., and Coauthors, 2019: Observing Hurricane Harvey's eyewall at
390 landfall. *Bull. Am. Meteorol. Soc.*, doi:10.1175/BAMS-D-17-0237.1.
391 Giammanco, I. M., J. L. Schroeder, and M. D. Powell, 2012: GPS Dropwindsonde and WSR-
392 88D Observations of Tropical Cyclone Vertical Wind Profiles and Their Characteristics.
393 *Weather Forecast.*, **28**, 77–99, doi:10.1175/waf-d-11-00155.1.
394 Hirth, B. D., J. L. Schroeder, C. C. Weiss, D. a. Smith, and M. I. Biggerstaff, 2012: Research
395 Radar Analyses of the Internal Boundary Layer over Cape Canaveral, Florida, during the
396 Landfall of Hurricane Frances (2004). *Weather Forecast.*, **27**, 1349–1372,
397 http://doi:10.1175/WAF-D-12-00014.1.
398 Hlywiak, J., and D. S. Nolan, 2022: The Evolution of Asymmetries in the Tropical Cyclone
399 Boundary Layer Wind Field during Landfall. *Mon. Wea. Rev.*, **150**, 529–549,
400 https://doi.org/10.1175/MWR-D-21-0191.1.
401 Jaimes, B., L.K. Shay, and E.W. Uhlhorn, 2015: Enthalpy and Momentum Fluxes during
402 Hurricane Earl Relative to Underlying Ocean Features. *Mon. Wea. Rev.,* **143**, 111–131,
403 https://doi.org/10.1175/MWR-D-13-00277.1
404 Kepert, J., 2001: The Dynamics of Boundary Layer Jets within the Tropical Cyclone Core . Part
405 I : Linear Theory. *J. Atmos. Sci.*, **58**, 2469–2484, doi:10.1175/1520-
406 0469(2001)058<2469:TDOBLJ>2.0.CO;2.
407 Kepert, J., and Y. Wang, 2001: The Dynamics of Boundary Layer Jets within the Tropical
408 Cyclone Core. Part II: Nonlinear Enhancement. *J. Atmospheric Sci.*, **58**, 2485–2501,
409 https://doi.org/10.1175/1520-0469(2001)058<2485:TDOBLJ>2.0.CO;2.

Klotz, B. W., and H. Jiang, 2017: Examination of Surface Wind Asymmetries in Tropical Cyclones. Part I: General Structure and Wind Shear Impacts. *Mon. Wea. Rev.*, **145**, 3989–4009, https://doi.org/10.1175/MWR-D-17-0019.1.

Kosiba, K. A., and J. Wurman, 2014: Finescale dual-Doppler analysis of hurricane boundary layer structures in hurricane Frances (2004) at landfall. *Mon. Weather Rev.*, **142**, 1874–1891, doi:10.1175/MWR-D-13-00178.1.

Lorsolo, S., J. L. Schroeder, P. Dodge, and F. Marks, 2008: An Observational Study of Hurricane Boundary Layer Small-Scale Coherent Structures. *Mon. Weather Rev.*, **136**, 2871–2893, http://doi:10.1175/2008MWR2273.1.

Ming, J., J. A. Zhang, R.F. Rogers, F. D. Marks, Y. Wang, and N. Cai, 2014: Multiplatform observations of boundary layer structure in the outer rainbands of landfalling typhoons. *J. Geophys. Res. – Atmos.*, **119**, 7799-7814, https://doi: 10.1002/2014JD021637.

Ming, J., J.A. Zhang, and R.F. Rogers, 2015: Typhoon boundary layer structure from dropsonde composites. *J. Geophys. Res.*, **120**(8):3158-3172, https://doi:10.1002/2014JD022640.

Ming, J., R. Liu, J.A. Zhang, and R.F. Rogers, 2022: The shear-relative variation of inflow angle and its relationship to tropical cyclone intensification. *J. Geophys. Res. – Atmos.* , **127**, https://doi.org/10.1029/2022JD037280.

Montgomery, M. T., J. A. Zhang, and R. K. Smith, 2014: An analysis of the observed low-level structure of rapidly intensifying and mature hurricane Earl (2010). *Q. J. R. Meteorol. Soc.*, **140**, 2132–2146, doi:10.1002/qj.2283.

Ooyama, K. V., 1969: Numerical simulation of the life cycle of tropical cyclones. *J. Atmos. Sci.*, **26**, 3–40.

Reasor, P., R.F. Rogers, and S. Lorsolo, 2013: Environmental flow impacts on tropical cyclone structure diagnosed from airborne Doppler radar composites. *Mon. Wea. Rev*., **141**, 2949-2969.

Rogers R.F., and E. Uhlhorn, 2008: Observations of the structure and evolution of surface and flight-level wind asymmetries in Hurricane Rita (2005). *Geophysical Research Letters*, **35**, L22811, doi:10.1029/2008GL034774.

Rogers, R.F., S. Lorsolo, P. Reasor, J. Gamache, F.D. Marks, Jr., 2012: Multiscale analysis of tropical cyclone kinematic structure from airborne Doppler radar composites. *Monthly Weather Review*, **140**, 77-99.

Sanger, N. T., M. T. Montgomery, R. K. Smith, and M. M. Bell, 2014: An observational study of tropical cyclone spinup in Supertyphoon Jangmi (2008) from 24 to 27 September. *Mon. Wea. Rev*., **142**, 3–28, doi:10.1175/MWR-D-12-00306.1.

Shapiro, L. J., and H. E. Willoughby, 1982: The response of balanced hurricanes to local sources of heat and momentum. *J. Atmos. Sci.*, **39,** 378–394.

Shay, L.K., G.J. Goni, and P.G. Black, 2000: Effects of a Warm Oceanic Feature on Hurricane Opal. *Mon. Wea. Rev.,* **128**, 1366–1383, https://doi.org/10.1175/1520-0493(2000)128<1366:EOAWOF>2.0.CO;2

Smith, R. K., and M. T. Montgomery, 2015: Towards clarity on understanding tropical cyclone intensification. *J. Atmos. Sci*., **72**, 3020-3031.

Smith, R. K., and M. T. Montgomery, 2016: The efficiency of diabatic heating and tropical cyclone intensification. *Quart. J. Roy. Meteor. Soc*., **142**, 2081–2086.

Smith, R. K., M. T. Montgomery, and N. Van Sang, 2009: Tropical cyclone spin-up revisited. *Quart. J. Roy. Meteor. Soc*., **135**, 1321–1335, https://doi.org/10.1002/qj.428.

455 Smith, R. K., G. Kilroy and M. T. Montgomery, 2021: Tropical cyclone life cycle in a three-
456 dimensional numerical simulation. Quart. J. Royal Meteorol. Soc, 147, 3373-3393.
457 Sun Z, Zhang B, Zhang JA, Perrie W. Examination of Surface Wind Asymmetry in Tropical
458 Cyclones over the Northwest Pacific Ocean Using SMAP Observations. *Remote Sensing*.
459 2019; 11(22):2604. https://doi.org/10.3390/rs11222604
460 Ueno, M., and M. Kunii, 2009: Some aspects of azimuthal wavenumber-one structure of
461 typhoons represented in the JMA operational mesoscale analyses. *J. Meteor. Soc. Japan*, **87**,
462 615–633.
463 Ueno, M., and K. Bessho, 2011: A statistical analysis of near-core surface wind asymmetries in
464 typhoons obtained from QuikSCAT data. *J. Meteor. Soc. Japan*, **89**, 225–241.
465 Uhlhorn, E. W., B. W. Klotz, T. Vukicevic, P. D. Reasor, and R. F. Rogers, 2014: Observed
466 Hurricane Wind Speed Asymmetries and Relationships to Motion and Environmental Shear.
467 *Mon. Wea. Rev*., **142**, 1290–1311, https://doi.org/10.1175/MWR-D-13-00249.1
468 Wadler, J. B., J. A. Zhang, R. F. Rogers, B. Jaimes, and L. K. Shay, 2021: The Rapid
469 Intensification of Hurricane Michael (2018): Storm Structure and the Relationship to
470 Environmental and Air-Sea Interactions. *Mon. Wea. Rev*., **149**, 245-267.
471 Wurman, J., and J. Winslow, 1998: Intense sub-kilometer-scale boundary layer rolls observed in
472 hurricane Fran. *Science (80-.).*, **280**, 555–557, doi:10.1126/science.280.5363.555.
473 Wurman, J., & Kosiba, K., 2018. The role of small-scale vortices in enhancing surface winds and
474 damage in Hurricane Harvey (2017). *Monthly Weather Review*, **146**(3), 713– 722.
475 https://doi.org/10.1175/MWR-D-17-0327.1

476 Zhang, J. A., & Uhlhorn, E. W., 2012. Hurricane Sea Surface Inflow Angle and an Observation-
477 Based Parametric Model. *Monthly Weather Review*, **140**(11), 3587-3605.
478 https://doi.org/10.1175/MWR-D-11-00339.1
479 Zhang, J.A., R.F. Rogers, D.S. Nolan, and F.D. Marks, Jr., 2011: On the characteristic height
480 scales of the hurricane boundary layer. *Monthly Weather Review*, **139**, 2523-2535.1
481 Zhang, J.A., R.F. Rogers, P. Reasor, E. Uhlhorn, and F.D. Marks, Jr., 2013: Asymmetric
482 hurricane boundary layer structure from dropsonde composites in relation to the
483 environmental wind shear. *Mon. Wea. Rev*., **141**, 3968–3984.
484 Zhang, J.A., D.S. Nolan, R.F. Rogers, and V. Tallapragada, 2015: Evaluating the Impact of
485 Improvements in the Boundary Layer Parameterization on Hurricane Intensity and Structure
486 Forecasts in HWRF. *Mon. Wea. Rev*., **143**, 3136-3155.
487 Zhang, J.A., R.F. Rogers, and V. Tallapragada, 2017: Impact of Parameterized Boundary Layer
488 Structure on Tropical Cyclone Rapid Intensification Forecasts in HWRF. *Mon. Wea. Rev*.,
489 **145**, 1413–1426, doi: 10.1175/MWR-D-16-0129.1.
490 Zhang, J.A. R.F. Rogers, P.D. Reasor, and J.F. Gamache, 2023: The Mean Kinematic Structure
491 of the Tropical Cyclone Boundary Layer and Its Relationship to Intensity Change. *Mon. Wea.*
492 *Rev*., **151**, 63-84, https://doi.org/10.1175/MWR-D-21-0335.1.
493 Zhu, P., J.A. Zhang, and F.J. Masters, 2010: Wavelet analyses of turbulence in the hurricane
494 surface layer during landfalls. *Journal of the Atmospheric Sciences*, **67**(12):3793-3805,
495 https://doi.org/10.1175/2010JAS3437.1

496